



Controllable morphology CoFe₂O₄/g-C₃N₄ p-n heterojunction photocatalysts with built-in electric field enhance photocatalytic performance

Wei He^a, Liang Liu^b, Tingting Ma^a, Huimin Han^b, Jiajing Zhu^b, Yingpei Liu^b, Zheng Fang^a, Zhao Yang^b, Kai Guo^{a,c,*}

^a College of Biotechnology and Pharmaceutical Engineering, Nanjing Tech University, Nanjing 211816, PR China

^b College of Engineering, China Pharmaceutical University, Nanjing 211198, PR China

^c State Key Laboratory of Materials-Oriented Chemical Engineering, Nanjing Tech University, Nanjing 210009, PR China

ARTICLE INFO

Keywords:

P-n heterojunction
Morphology
Acousto-optic microreactor
Photocatalysis
CoFe₂O₄/g-C₃N₄

ABSTRACT

CoFe₂O₄/g-C₃N₄ p-n heterojunction photocatalysts have been successfully synthesized. The formation of p-n heterojunction and the unique morphology of g-C₃N₄ enhanced electron transfer and charge separation, leading to a significant improvement in photocatalytic efficiency. 5-CoFe₂O₄/CNS not only had a high photocatalytic hydrogen evolution rate of 18.9 mmol·g⁻¹·h⁻¹, but also possessed an efficient photocatalytic fluoroquinolone antibiotics removal efficiency. A smaller band gap in 5-CoFe₂O₄/CNS photocatalyst promoted more light generated electrons under visible light irradiation. An internal electric field at the contact interface accelerated the accumulation of electrons and holes in the valence band of g-C₃N₄ and conduction band of CoFe₂O₄, thereby revealing a higher separation efficiency and noticeable inhibited recombination rate of the photoinduced electrons and holes. Also, improved removal efficiency for fluoroquinolone antibiotics was attained in the self-designed acousto-optic microreactor, which was 7.2 and 30 times higher than quartz glass tube and batch experiment, respectively.

1. Introduction

As a n-type semiconductor with a non-metal polymeric structure, g-C₃N₄ has a narrow band gap of 2.7 eV [1]. Thus, it may have capacity to harvest the solar spectrum and serve as a visible light-driven photocatalyst for the degradation of organic contaminants. Moreover, the reliable chemical inertness, low toxicity and cost effectiveness of g-C₃N₄ make it an striking photocatalytic catalyst [2]. Unfortunately, owing to the stacked sheet structure and the low transfer efficiency of photoinduced carriers, inefficient utilization of visible-light and small specific surface area significantly limit its photocatalytic performance [3,4]. Therefore, many modifications have been applied to enhance the photocatalytic activity of g-C₃N₄, such as metal doping (Au [5], Na [6], Ag [7], Fe [8]), non-metal doping (B [9], F [10], C [11,12], P [13], O [14]) and combination with other semiconductors [12,15,16]. Heterojunctions based on g-C₃N₄ including TiO₂/g-C₃N₄ [17], Fe₂O₃/g-C₃N₄ [18], NH₂-UiO-66/g-C₃N₄ [19], WO₃/g-C₃N₄ [20] and Co₃O₄@-CoO/g-C₃N₄ [21] have been employed to enhance light absorption as

well as photogenerated electron-hole pair separation. In addition, the surface area of g-C₃N₄ could be greatly enhanced with unique morphologies [22]. The surface charge and morphology, such as nano sheet, nanotube and porous structure, would also have an impact on the photocatalytic activity of the materials [23,24].

Spinel ferrites, MFe₂O₄ (M = Fe, Mn, Co, Ni, Cu, Zn), have recently attracted tremendous attention in catalysis owing to their environmental compatibility and stability as well as their easy synthesis [25]. A p-type semiconductor referred to as CoFe₂O₄, with a relatively narrow band gap of 1.33 eV [26,27], has been applied in various fields, particularly in electronics and catalysis [28,29]. Currently, Z-scheme CoFe₂O₄/g-C₃N₄ heterojunctions have been widely used in the pollutant degradation [30], Li-O₂ batteries [31], Hg (II) reduction [32], oxygen evolution reaction [33], nitrogen fixation [34]. However, there are relatively few reports concerning CoFe₂O₄/g-C₃N₄ p-n heterojunctions in the photocatalytic process. Their perfect matching between the conduction band (CB) and valence band (VB) may enhance the efficiency of photoinduced charge separation under visible light irradiation when

* Corresponding author at: College of Biotechnology and Pharmaceutical Engineering, Nanjing Tech University, Nanjing 211816, PR China.

E-mail addresses: yzcpu@cpu.edu.cn (Z. Yang), guok@njtech.edu.cn (K. Guo).

<https://doi.org/10.1016/j.apcatb.2022.121107>

Received 31 August 2021; Received in revised form 16 December 2021; Accepted 14 January 2022

Available online 19 January 2022

0926-3373/© 2022 Elsevier B.V. All rights reserved.

$\text{CoFe}_2\text{O}_4/\text{g-C}_3\text{N}_4$ p-n heterojunctions are formed.

Hybrid technologies including two or more techniques are gaining interest for environmental chemical engineering and catalysis [35]. Acoustic cavitation can not only enhance the dispersion of photocatalyst particles, but also clean the photocatalyst surface, creating more active sites on its surface and improving the mass transfer between solution phase and catalyst [36]. In addition, micro-flow technique is a versatile alternative to traditional batch process due to several notable advantages, including improved mixing efficiency, superior heat transfer, safer handling of hazardous reagents, and a more straightforward path to scale-up [37]. So far, photocatalytic process in a microreactor [38] or under ultrasound irradiation [39] has been reported. The flow of sound generated by ultrasonic waves and the instantaneous collapse of cavitation bubbles will cause confusion of the solution, so that the surface of the catalyst can be cleaned to maintain more active sites for the reaction [40]. Continuous flow characteristics of the microreactor will also weaken the enrichment of hazardous substance on the surface of the catalyst [41]. The ultrasonic shock, sound flow and pitting phenomenon of the catalyst surface under ultrasonic irradiation, as well as scale effect in the microreactor will enhance the mass transfer rate between the reactants, free radicals in the liquid phase and the solid surface of the catalyst synergistically [42]. It is anticipated that an acousto-optic microreactor developed in this study for the first time consisting of photocatalysis and ultrasound irradiation in a continuous flow mode will not only improve the photocatalytic efficiency, but also prevent photocatalyst deactivation.

In this study, p-n $\text{CoFe}_2\text{O}_4/\text{g-C}_3\text{N}_4$ heterojunctions were fabricated via a facile one-pot coprecipitation process. These heterojunctions were evaluated to reveal the role of surface charge and morphology on the catalytic activity of photocatalysts both in photocatalytic degradation and H_2 evolution. A self-design acousto-optic microreactor was fabricated and applied in the photocatalytic degradation process to evaluate the role of reaction technique in the degradation process. The structures of p-n heterojunctions were confirmed by catalyst characterizations. The optical and electrochemical properties were characterized by UV-vis spectroscopy, photoluminescence (PL) emission spectroscopy, transient photocurrent responses and Mott-Schottky curve. In addition, the degradation kinetics of ciprofloxacin (CIP) were investigated. Based on the results of reactive species trapping experiments and HPLC/Q-TOFMS results, the primary reactive species, degradation pathways and possible degradation mechanism during the degradation of CIP were proposed.

2. Materials and methods

2.1. Synthesis of photocatalysts

CoFe_2O_4 magnetic nanoparticles were anchored on various morphologies $\text{g-C}_3\text{N}_4$ via a coprecipitation method [43]. The detailed synthetic process of $\text{g-C}_3\text{N}_4$ and CoFe_2O_4 were shown in Section 1.2 and 1.3 of Supporting Information. Bulk $\text{g-C}_3\text{N}_4$, $\text{g-C}_3\text{N}_4$ nanotubes, $\text{g-C}_3\text{N}_4$ nanosheets and mesoporous $\text{g-C}_3\text{N}_4$ were named as BCN, CNT, CNS and MCN. Typically, certain volumes of 0.1 M $\text{Fe}(\text{NO}_3)_3 \cdot 9\text{H}_2\text{O}$ and $\text{Co}(\text{NO}_3)_2 \cdot 6\text{H}_2\text{O}$ (0.1 M) were added into 50 mL water containing 150 mg BCN. After ultrasonic dispersion for 1 h, 10 mL $(\text{NH}_4)_2\text{CO}_3$ (0.5 M) was added dropwise into the mixture and stirred for 15 min. And then, the above suspension was transferred into a three-necked flask and refluxed at 100 °C for 1 h. The obtained precursor was washed and dried at 60 °C overnight. Finally, the resulting solid was calcined at 300 °C for 2.5 h to obtain $\text{CoFe}_2\text{O}_4/\text{BCN}$. According to the weight ratios of CoFe_2O_4 in the heterojunctions (1 wt%, 3 wt%, 5 wt%, 10 wt%, 20 wt%, 30 wt% and 40 wt%, respectively), the obtained products were noted as 1- $\text{CoFe}_2\text{O}_4/\text{BCN}$, 3- $\text{CoFe}_2\text{O}_4/\text{BCN}$, 5- $\text{CoFe}_2\text{O}_4/\text{BCN}$, 10- $\text{CoFe}_2\text{O}_4/\text{BCN}$, 20- $\text{CoFe}_2\text{O}_4/\text{BCN}$, 30- $\text{CoFe}_2\text{O}_4/\text{BCN}$ and 40- $\text{CoFe}_2\text{O}_4/\text{BCN}$, respectively.

In addition, 5 wt% of $\text{CoFe}_2\text{O}_4/\text{g-C}_3\text{N}_4$ nanotubes (5- $\text{CoFe}_2\text{O}_4/\text{CNT}$), 5 wt% $\text{CoFe}_2\text{O}_4/\text{g-C}_3\text{N}_4$ nanosheets (5- $\text{CoFe}_2\text{O}_4/\text{CNS}$) and 5 wt%

$\text{CoFe}_2\text{O}_4/\text{mesoporous g-C}_3\text{N}_4$ (5- $\text{CoFe}_2\text{O}_4/\text{MCN}$) were synthesized via the same method as $\text{CoFe}_2\text{O}_4/\text{BCN}$. The overall procedures for the synthesis of the $\text{CoFe}_2\text{O}_4/\text{g-C}_3\text{N}_4$ with different morphologies was presented in Fig. 1. The characterizations of photocatalyst were illustrated in Section 1.4 of Supporting Information.

2.2. Photocatalytic degradation

Photocatalytic degradation experiments with a series of $\text{CoFe}_2\text{O}_4/\text{g-C}_3\text{N}_4$ photocatalysts were conducted under visible light. A 250 W xenon lamp with a 420 nm cut-off filter was employed as the visible light irradiation source. Continuous flow degradation experiments were performed in a quartz glass tube and the acousto-optic microreactor (Fig. S2), respectively. When the quartz glass tube (internal diameter = 1 mm, volume = 0.4 mL) was used as the microreactor, the suspension containing photocatalyst and CIP water solution was injected into the microreactor at constant flow rate. Different residence times (2, 4, 8, 10, 12, 15, 20 min) were tested by changing the liquid flow rate (0.2, 0.1, 0.05, 0.04, 0.033, 0.027, 0.02 mL/min). For the acousto-optic microreactor, degradation experiments were carried out in the same way as the quartz glass tube, and the frequency of two ultrasonic generators were locked at 100 Hz. The liquid flow rates were changed (11.360, 5.680, 3.787, 2.272, 1.420, 1.136, 0.568, 0.379, 0.284, 0.227 mL/min) to test different residence times (0.1, 0.2, 0.3, 0.5, 0.8, 1, 2, 3, 4, 5 min). After flowing through the microchannel with the reaction suspension for twice, the Xenon lamp with a 420 nm cut-off filter was turned on.

The detailed implementation steps of the microreactor were presented in the Fig. S3 and Fig. S4. Typically, a 250 W Xenon lamp with a 420 nm cut-off filter and the microreactor were placed on the same horizontal surface. The distance was set to 15 cm. Before the reaction, the height of the microreactor was adjust to ensure that the light spot ($d = 5$ cm) was completely placed on the microreactor.

The dominated reactive oxygen species (ROS) of the $\text{CoFe}_2\text{O}_4/\text{g-C}_3\text{N}_4$ detected during radical scavenging experiments were determined through the addition of specific ROS scavengers prior to photocatalytic degradation process. The scavengers included 4-hydroxy-2,2,6,6-tetramethylpiperidinyloxy (TEMPOL, 10 mM) for the superoxide iron radical ($\cdot\text{O}_2^-$), isopropanol (IPA, 10 mM) for the hydroxyl radical ($\cdot\text{OH}$) and sodium oxalate ($\text{Na}_2\text{C}_2\text{O}_4$, 10 mM) for photogenerated holes (h^+), respectively [44,45].

2.3. Photocatalytic H_2 evolution

The photocatalytic H_2 evolution experiments were conducted in the Labsolar-6A photocatalytic test device (Beijing Perfect light Technology Co., Ltd.). Typically, the aqueous solution (100 mL) containing triethanolamine (TEOA, 10 wt%), chloroplatinic acid (1 wt%, respect to Pt) and solid catalyst (50 mg) was added into the flask. The mixture was dispersed under ultrasound irradiation for 10 min. After replaced with nitrogen gas, the flask was vacuumized several times to remove air completely. Then the flask was placed in the photocatalytic test device to evaluate the H_2 evolution performances of these four catalysts (5- $\text{CoFe}_2\text{O}_4/\text{BCN}$, 5- $\text{CoFe}_2\text{O}_4/\text{MCN}$, 5- $\text{CoFe}_2\text{O}_4/\text{CNT}$, 5- $\text{CoFe}_2\text{O}_4/\text{CNS}$). The reaction liquid was irradiated under vigorous stirring conditions by a Xenon lamp (300 W) with a UV cutoff filter (UVCUT420, $\lambda > 420$ nm). The illumination intensity in this study was 150 mW/cm². The temperature inside the reaction liquid was maintained at 25 °C. Gas chromatograph (GC9790II) equipped with a thermal conductivity detector was used for on-line monitoring of the generated hydrogen.

3. Results and discussion

3.1. p-n heterojunction induced via the morphology of $\text{g-C}_3\text{N}_4$

The transmission electron microscopy (TEM) measurement was introduced to study the internal structure of 5- $\text{CoFe}_2\text{O}_4/\text{BCN}$, 5-



Fig. 1. Synthesis route of composites photocatalyst.

CoFe₂O₄/MCN, 5-CoFe₂O₄/CNS and 5-CoFe₂O₄/CNT. The pictures were shown in Fig. 2a-d. The 5-CoFe₂O₄/BCN revealed a large black shadow generated by the typical stacked structure (Fig. 2a). Compared with 5-CoFe₂O₄/BCN, 5-CoFe₂O₄/MCN possessed stacked structure with many pores (Fig. 2b), which was in consistent with the above SEM results. Fig. 2c verified that 5-CoFe₂O₄/CNS was thinner than 5-CoFe₂O₄/BCN and 5-CoFe₂O₄/MCN, and there was no obvious stacked structure. Besides, the regular lattice structure with the d spacing of 0.25 nm was observed in the HRTEM image, which was assigned to CoFe₂O₄. For 5-CoFe₂O₄/CNT, TEM measurement further confirmed that the desired tubular structure was successfully obtained, and CoFe₂O₄ was uniformly deposited on CNT (Fig. 2d). The morphology feature of 5-CoFe₂O₄/CNS was then verified by atomic force microscopy (AFM) characterization. As illustrated in Fig. 2e and 2f, the layered structure could be seen clearly in the AFM image. The thickness of CNS was around 2 nm (Fig. 2e and 2f, inset), which was similar with the results in the literature

[44]. Furthermore, the diameter of CoFe₂O₄ was around 2–3 nm.

The results of powder X-ray diffraction (Fig. S5), elemental mapping images (Fig. S6) and Fourier transform infrared spectra (Fig. S8) revealed that the resulting solid photocatalysts consisted of g-C₃N₄ with different morphologies and CoFe₂O₄. Interestingly, X-ray photoelectron spectroscopy (XPS) analysis of BCN and 5-CoFe₂O₄/BCN indicated the opposite drift phenomenon (Fig. S7). Surface electron density was negatively correlated with XPS binding energy [45,46]. The electron screening effect would be higher with the increasing of electron density, thereby resulting in the reduced binding energy. XPS analysis indicated that electrons might transfer from g-C₃N₄ to CoFe₂O₄ during the synthesis of CoFe₂O₄/g-C₃N₄ composites. Therefore, the above XPS results confirmed the formation of a CoFe₂O₄/g-C₃N₄ heterojunction and the existence of a strong interaction between CoFe₂O₄ and g-C₃N₄. To our surprise, not all kinds of CoFe₂O₄/g-C₃N₄ could form the p-n heterojunction. As shown in Fig. 3a-d, Mott-Schottky (M-S) plot of

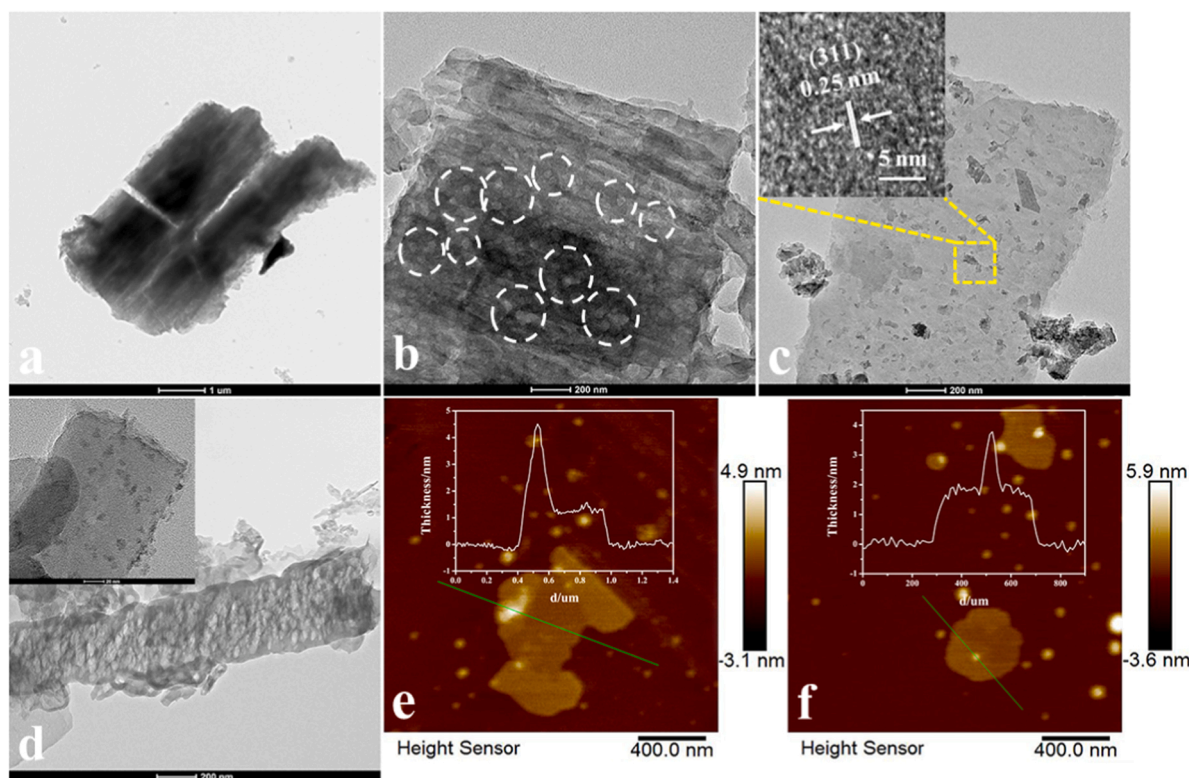


Fig. 2. TEM images of 5-CoFe₂O₄/BCN (a), 5-CoFe₂O₄/MCN (b), 5-CoFe₂O₄/CNS (c) (inset: HRTEM of 5-CoFe₂O₄/CNS), 5-CoFe₂O₄/CNT (d) and AFM images of 5-CoFe₂O₄/CNS (e-f).

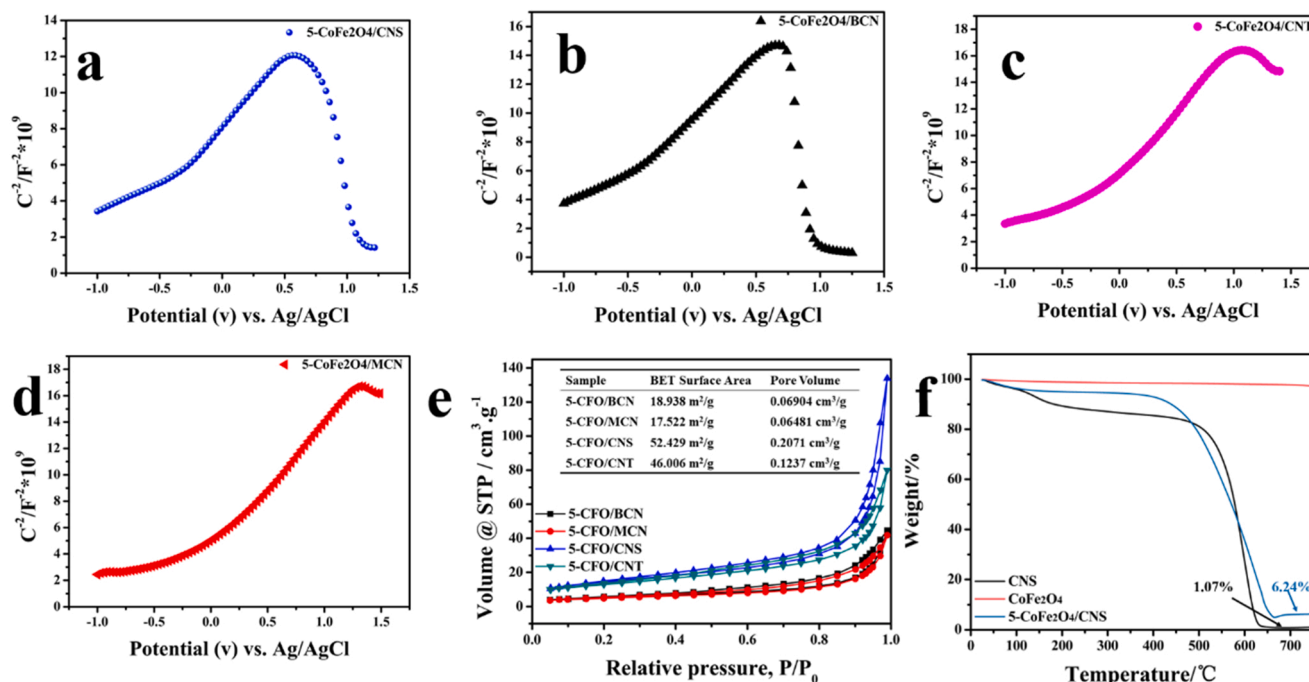


Fig. 3. Mott-Schottky plots of 5-CoFe₂O₄/BCN(a), 5-CoFe₂O₄/BCN (b), 5-CoFe₂O₄/CNT (c) and 5-CoFe₂O₄/MCN (d), N₂ adsorption-desorption isotherm plots of the samples (e) and the thermogravimetric analysis of CNS, CoFe₂O₄ and 5-CoFe₂O₄/CNS (f).

5-CoFe₂O₄/BCN presented the similar trend as 5-CoFe₂O₄/CNS, while two other plots (5-CoFe₂O₄/MCN and 5-CoFe₂O₄/CNT) showed an incomplete state in the negative slope port, which might indicate the unsuccessful formation of p-n heterojunction.

To investigate the surface areas of the as-prepared 5-CoFe₂O₄/g-C₃N₄ samples, the N₂ adsorption-desorption isotherms were evaluated. As shown in Fig. 3e, all the samples presented a type IV isotherm with a narrow hysteresis loops which was the characteristic curve in mesoporous materials [29]. The surface areas obtained by the Brunauer-Emmett-Teller method [47] were 18.938, 17.522, 52.429 and 46.006 m²/g for 5-CoFe₂O₄/BCN, 5-CoFe₂O₄/MCN, 5-CoFe₂O₄/CNS and 5-CoFe₂O₄/CNT, respectively (Fig. 3e, insert). In addition, the pore volume of the 5-CoFe₂O₄/CNS attained 0.2071 cm³/g, which was about 3.0-fold higher than the 5-CoFe₂O₄/BCN (0.06904 cm³/g). All these findings demonstrated that the 5-CoFe₂O₄/CNS had a larger specific surface area. Larger specific area was beneficial for photocatalytic adsorption, the diffusion of reactants towards active site and the mass transfer, promoting the ROS attack.

Owing to the fact that g-C₃N₄ would decompose rapidly under 600 °C [48], thermogravimetric analysis was employed to verify the actual content of CNS in the 5-CoFe₂O₄/CNS. As shown in Fig. 3f, the weight of pure CoFe₂O₄ hardly decreased during the heating process, while the weight of pure CNS dropped to 1.07% of the original weight. Based on the results of pure CoFe₂O₄ and CNS, the thermogravimetric analysis of 5-CoFe₂O₄/CNS was tested. The remaining substances after the heating process included CoFe₂O₄ and indecomposable substances of CNS. The content of CoFe₂O₄ in 5-CoFe₂O₄/CNS was calculated to be 5.17%. Accordingly, the content of CNS was 94.83%, which agreed with component proportion in the synthetic process.

3.2. Enhanced photocatalytic performance via p-n heterojunction

For 5 wt% CoFe₂O₄/Bulk g-C₃N₄, 69.4% of CIP could be removed within 60 min visible illumination (Fig. S9a), whereas only 33.7% and 42.7% CIP were degraded in 60 min for pure Bulk g-C₃N₄ and CoFe₂O₄, respectively. To investigate the effect of different morphologies on the photocatalytic activity of CoFe₂O₄/g-C₃N₄, g-C₃N₄ with different

morphologies ranging from one-dimensional to three-dimensional were coupled with CoFe₂O₄. The mass ratio of CoFe₂O₄ in CoFe₂O₄/g-C₃N₄ photocatalysts was set to be 5 wt%. The results were summarized in Fig. 4a. The photocatalytic removal efficiencies of MCN, CNS and CNT were much higher than that of BCN after 1 h reaction. Further, different samples exhibited different photodegradation properties, which were in order of 5-CoFe₂O₄/MCN < 5-CoFe₂O₄/BCN < 5-CoFe₂O₄/CNT < 5-CoFe₂O₄/CNS. Compared with g-C₃N₄-based conventional type II heterojunction [4] and g-C₃N₄-based Z-scheme heterojunction [30], 5-CoFe₂O₄/CNS p-n heterojunction revealed in this study for the first time also displayed excellent photocatalytic degradation.

The pseudo-first-order kinetic model with an equation of $\ln(C_0/C) = kt$ was introduced to deeply study the difference between CoFe₂O₄/g-C₃N₄ with different morphologies (Fig. 4b). From the kinetic curves and apparent rate constants, the 5-CoFe₂O₄/CNS presented the highest k value (0.0356 min⁻¹), which was about 2.33-fold higher than 5-CoFe₂O₄/MCN (0.0153 min⁻¹). The above-mentioned results were consistent with previous characterization analysis, confirming 5-CoFe₂O₄/CNS had optimum photocatalytic activity. Table S1 listed a comparison of the reported g-C₃N₄ photocatalysts for photocatalytic fluoroquinolone antibiotics removal. This data showed the superior photoactivity of 5-CoFe₂O₄/CNS than that of BiOBr/Carbon dots, Bi₂MoO₆, TiO₂/HNTs, TiO₂ nanorod modified g-C₃N₄ under visible-light irradiation.

These four heterojunctions (5-CoFe₂O₄/BCN, 5-CoFe₂O₄/MCN, 5-CoFe₂O₄/CNS and 5-CoFe₂O₄/CNT) were also evaluated in the photocatalytic H₂ evolution. Interestingly, the morphology of g-C₃N₄ showed a significant effect on the production of H₂. 5-CoFe₂O₄/MCN displayed the worst catalytic activity towards H₂ evolution. On the contrary, the yield of H₂ for 5-CoFe₂O₄/CNS (3784 μmol) was 2.6-fold (Fig. 4e) higher than that for 5-CoFe₂O₄/MCN (1457 μmol) when the reaction was set to be 4 h. The highest reaction rate was 946 μmol/h⁻¹ (18.9 mmol·g⁻¹·h⁻¹) which was 10-fold (Fig. 4f) higher than that of single CNS catalyst (93 μmol/h⁻¹) reported by Ajayan et al. [44] and even higher than ultrathin g-C₃N₄ nanosheets derived from direct thermal oxidation etching and ultrasonic exfoliation (12.16 mmol·g⁻¹·h⁻¹) [49]. Moreover, the catalytic activities of these

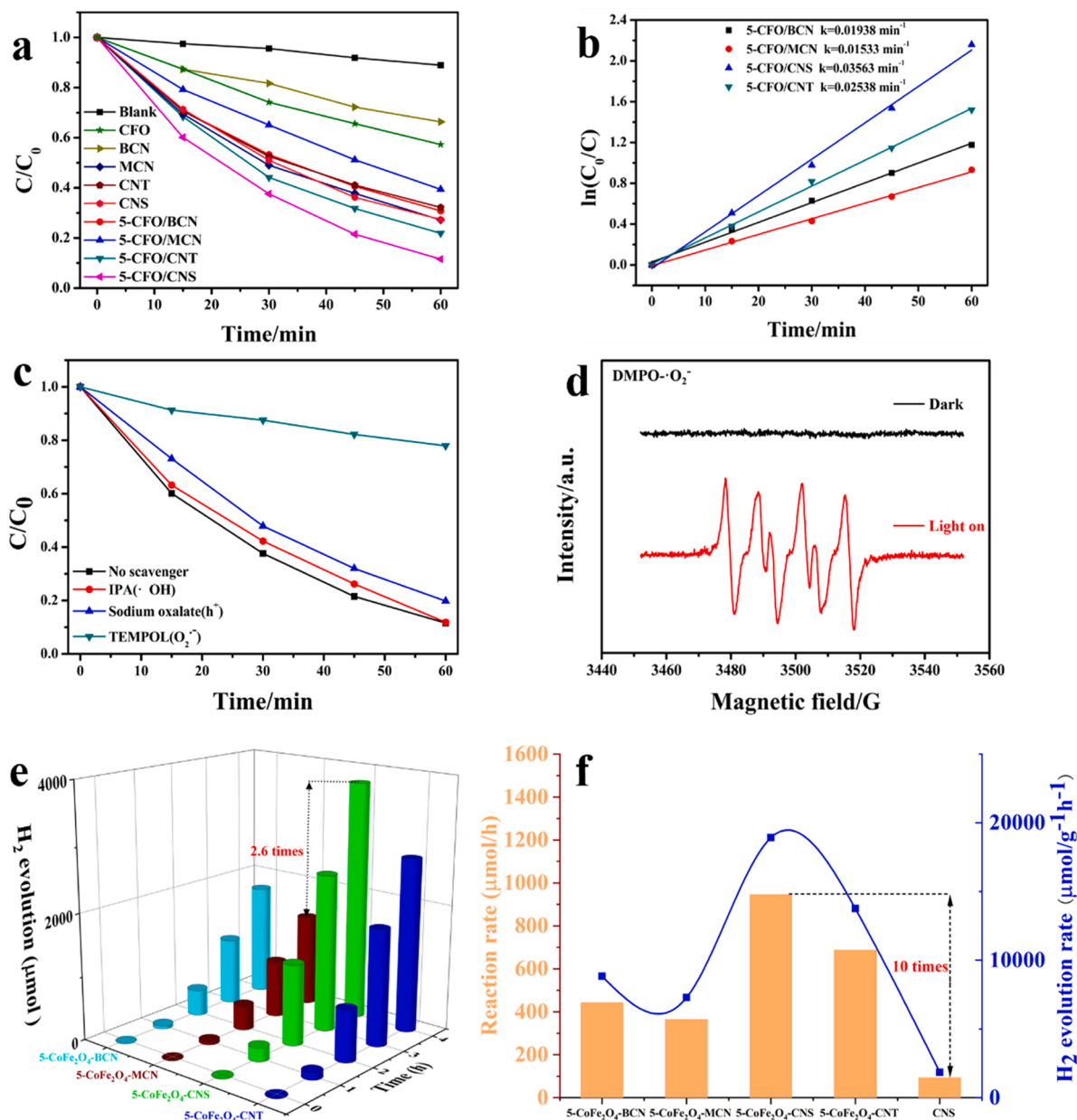


Fig. 4. The removal efficiency of CIP under different residence time (a) and $\ln(C/C_0)$ versus residence time (b) in batch mode, active radical scavenger experiments (c), room-temperature ESR spectra (d) with 5-CoFe₂O₄/CNS, the photocatalytic H₂ evolution performance (e) and reaction rate (f) of 5-CoFe₂O₄/BCN, 5-CoFe₂O₄/MCN, 5-CoFe₂O₄/CNS and 5-CoFe₂O₄/CNT.

four heterojunctions followed the same trend revealed in the photocatalytic degradation of fluoroquinolone antibiotics. Table S2 listed a comparison of the reported g-C₃N₄ photocatalysts for H₂-evolution performance. This data showed the superior photoactivity of 5-CoFe₂O₄/CNS than that of In³⁺, Pt/ZnIn₂S₄, Pt@Au nanorods, CNS, FeCoPOx nanowires, poly(benzotriazole) and Co(Mo-Mo₂C) modified g-C₃N₄ under visible-light irradiation.

As seen in Fig. 4c, the degradation of CIP was significantly inhibited (22.1%) due to the present of TEMPOL, while no obvious change was found with isopropanol. In other words, $\text{O}_2^{\cdot-}$ was the primary active species, which played a vital role in the degradation of CIP under visible light irradiation. Part of h^+ might directly oxidize CIP.

Room-temperature electron spin resonance (ESR) was also employed to further validate the ROS in the photodegradation of fluoroquinolone antibiotics (FQs) using 5,5-dimethyl-1-pyrroline N-oxide (DMPO) as radical spin trapping agent [2,25]. As shown in Fig. 4d, there was no

signal peak of $\text{DMPO}\cdot\text{O}_2^{\cdot-}$ appeared in the darkness, while obvious intensity signals could be detected under visible light. Therefore, $\text{O}_2^{\cdot-}$ was generated and played a significant role in the photocatalytic process based on the trapping experiments and ESR analysis.

Besides, the fresh and used 5-CoFe₂O₄/CNS were investigated by XPS and thermogravimetric analysis (Fig. S11). Fig. S11a displayed that XPS spectra of 5-CoFe₂O₄/CNS before and after reaction had no obvious changes. Furthermore, the used 5-CoFe₂O₄/CNS was also analyzed by thermogravimetric analysis. As shown in Fig. S11b, the remaining weight was in consistent with the fresh 5-CoFe₂O₄/CNS. All the results indicated that CoFe₂O₄/CNS remained stable after cycle use.

To further evaluate the potential of the 5-CoFe₂O₄/CNS for the photocatalytic degradation of FQs, other two FQs (enrofloxacin and norfloxacin) were selected as the substrates under visible light irradiation for 1 h (Fig. S9f). The removal efficiencies of enrofloxacin and norfloxacin were calculated to be 89.4% and 100%, respectively,

indicating 5-CoFe₂O₄/CNS p-n heterojunction had a wide applicability for FQs. To further study the reaction pathways, the oxidation products generated during the photocatalytic process were measured by HPLC/Q-TOFMS (positive ionization mode). The possible structural and molecular formulas were speculated via the mass spectrum and summarized in Fig. S13. Combined with the inferred intermediates and previous reports [50–53], five possible CIP degradation pathways were proposed in Fig. S12.

3.3. Enhanced photocatalytic degradation performance in the acousto-optic microreactor

To further enhance the photocatalytic performance of 5-CoFe₂O₄/CNS, the photocatalytic degradation experiments of CIP were evaluated in a quartz glass tube and a self-designed acousto-optic microreactor, respectively. All experimental conditions were consistent with the batch mode except reaction time. As shown in Fig. S2, the initial solution flowed into the microreactor from a PTFE tube. The degradation efficiency of CIP increased from 24.2% to 89.1% when the residence time increased from 2 to 15 min (Fig. 5a). And the removal efficiency showed a slight increase to 89.5% when the residence time was further increased to 20 min.

Moreover, the acousto-optic microreactor was also employed as the reactor to investigate the synergistic effect of sonolysis and photocatalysis. As the residence time increasing (Fig. 5c), the degradation efficiency of CIP increased rapidly from 15% to 91.0% in only 2 min and then finally reached 98.1% at 5 min (flow rate 227.2 $\mu\text{L}/\text{min}$), which was not only faster than batch reactor and quartz glass tube in terms of required degradation time, but also achieved a higher degradation efficiency. A high flow rate would reduce the contact time between visible light and photocatalysts in the solution, resulting in low reactive radical concentration in the solution and decreased the catalytic efficiency [54]. The continuous cleaning of the photocatalyst surface using ultrasonic vibrator might improve the mass transfer of pollutants between the

solution phase and catalyst, generating more active sites [36]. In addition, the continuous mode could improve mixing efficiency between reaction solution and visible light. As a result, the apparent rate constant of acousto-optic microreactor (1.07 min^{-1} , Fig. 5d) was about 7.2-fold higher than the quartz glass tube (0.149 min^{-1} , Fig. 5b). Furthermore, with the same photocatalyst used, the apparent rate constant of continuous mode (1.07 min^{-1} , Fig. 5d) was about 30-fold higher than the batch experiment (0.036 min^{-1} , Fig. 4c). Although exfoliated graphitic carbon nitride coated glass rings for micro pollutant removal is still a challenging technological solution [38], the quartz glass tube and self-designed acousto-optic microreactor used in this study were comparable with batch experiments. Better mass transfer between photocatalysts and substrates in the quartz glass tube would be beneficial to photocatalytic degradation compared with that in exfoliated graphitic carbon nitride coated glass rings.

3.4. Built-in electric field and charge transfer promoted via p-n heterojunction

Fig. 6a showed the UV–vis absorption spectra of the as-prepared samples. The light absorption range of BCN covered UV and partially visible light. For CoFe₂O₄/g-C₃N₄ composites, the spectra showed a weaker absorption edge than BCN ($\sim 550 \text{ nm}$) except 5-CoFe₂O₄/CNS, indicating that the heterojunction constructed by CoFe₂O₄ and CNS could effectively extend the spectral response to visible light. Since the states of C₃N₄ consisted of a sp^3 C-N δ -bond, a sp^2 C-N π -bond, and the lone pairs of bridged N atoms within the π -band, the multiple absorption peaks around 300–400 nm were attributed to the electron transitions from the lone pair to the antibonding δ^* -orbital, from the lone pair to the anti-bonding π^* -orbital, and from the conjugated π -orbital to the anti-bonding π^* -orbital [55]. In addition, the absorption within 440–600 nm was caused by defects [56] and the fast relaxation of electrons from the excited states to the ground state without the Stokes shift [55].

The band gap energies (Eg) of BCN and different CoFe₂O₄/g-C₃N₄

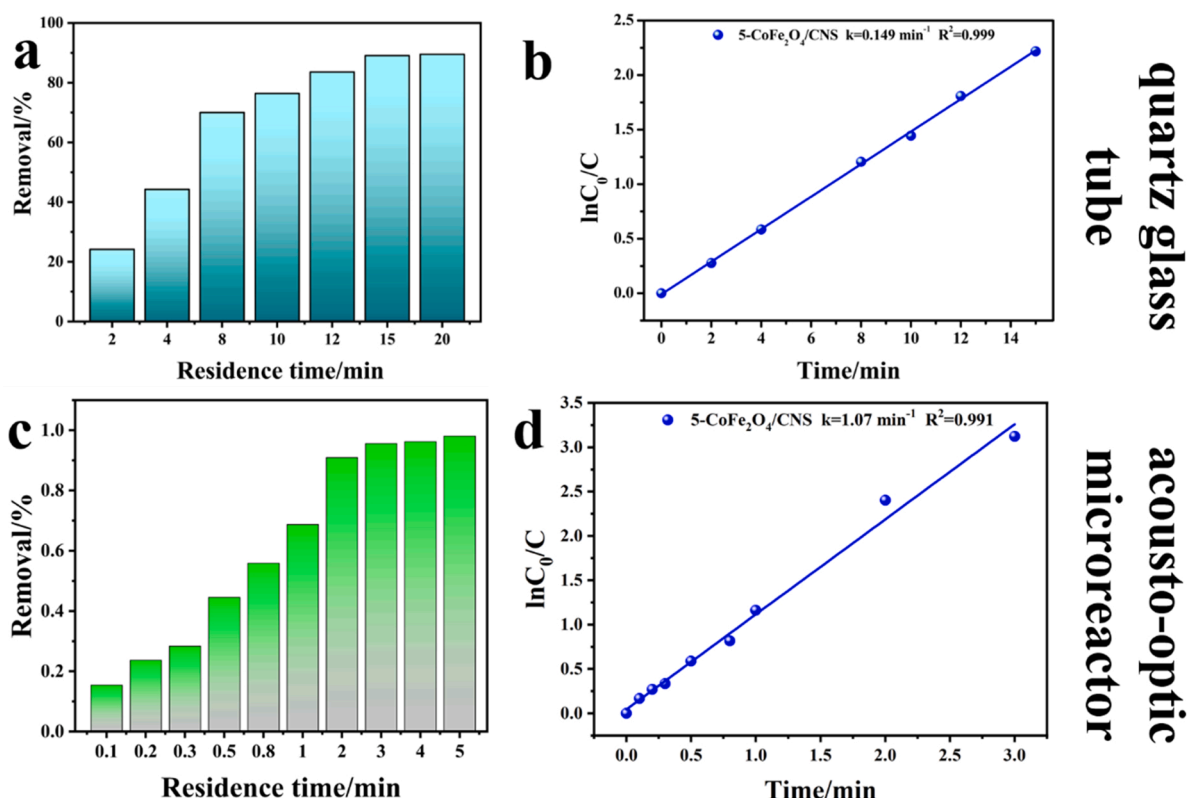


Fig. 5. The removal efficiency of CIP under different residence time (a, c) and $\ln(C/C_0)$ versus residence time (b, d).

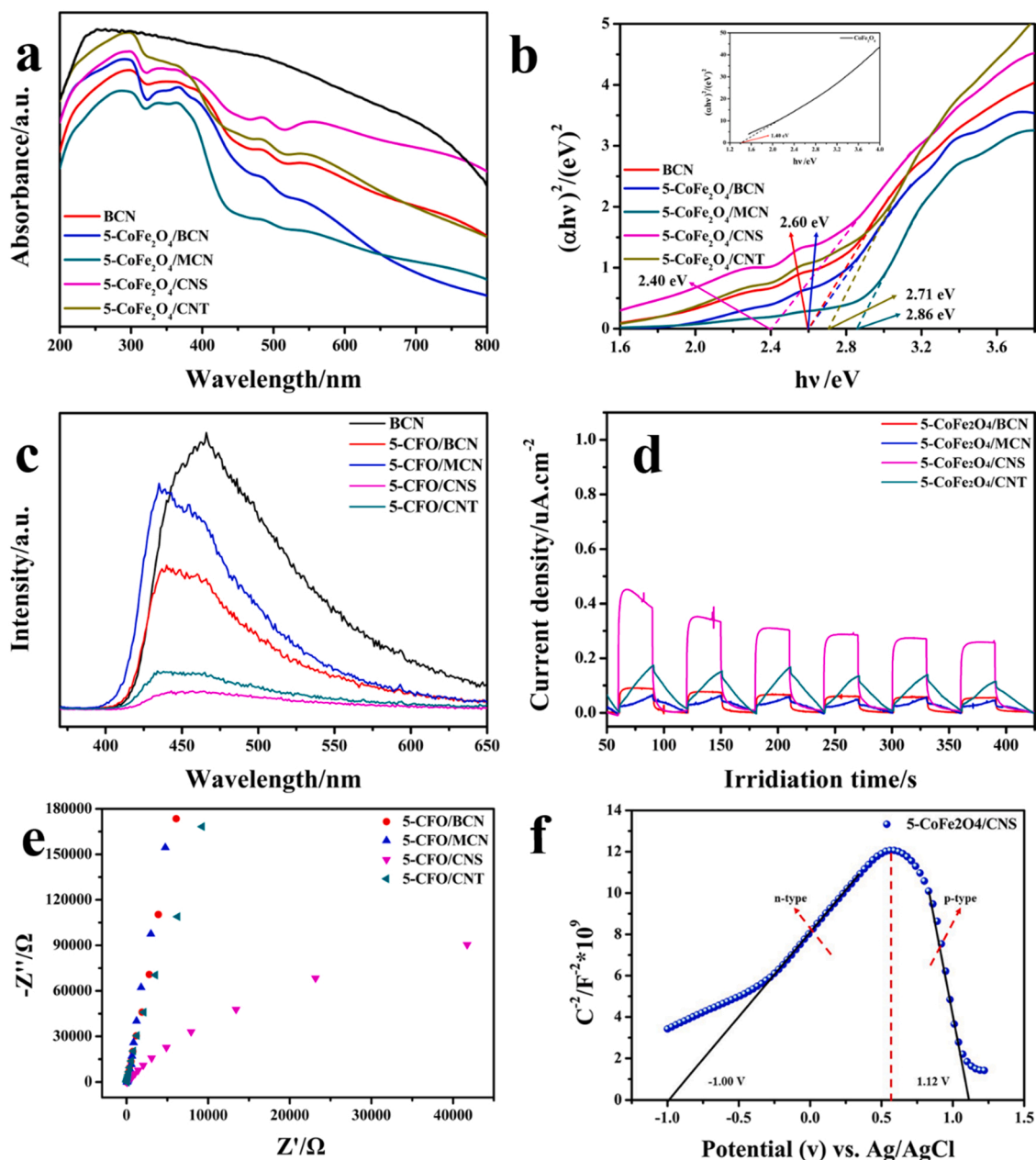


Fig. 6. UV-vis diffuse reflectance spectra (a) and corresponding Tauc plots of $(\alpha h\nu)^2$ versus $h\nu$ (b) of CoFe_2O_4 , BCN, 5- $\text{CoFe}_2\text{O}_4/\text{BCN}$, 5- $\text{CoFe}_2\text{O}_4/\text{MCN}$, 5- $\text{CoFe}_2\text{O}_4/\text{CNS}$ and 5- $\text{CoFe}_2\text{O}_4/\text{CNT}$, PL spectra (c), transient photocurrent responses (d), EIS Nyquist plots (e) of BCN, 5- $\text{CoFe}_2\text{O}_4/\text{BCN}$, 5- $\text{CoFe}_2\text{O}_4/\text{MCN}$, 5- $\text{CoFe}_2\text{O}_4/\text{CNS}$ and 5- $\text{CoFe}_2\text{O}_4/\text{CNT}$ and Mott-Schottky plot of 5- $\text{CoFe}_2\text{O}_4/\text{CNS}$ (f).

composites were calculated according to Eq. (1):

$$\alpha h\nu = A(h\nu - E_g)^{n/2} \quad (1)$$

where α , h , ν , A and E_g corresponded to the absorption coefficient, Planck's constant, light frequency, a constant and band gap energy [57], respectively. n was determined by the type of semiconductor optical transition ($n = 1$ for direct transition and $n = 4$ for indirect transition) [27]. The E_g of the as-prepared photocatalysts could be calculated from a plot of $(\alpha h\nu)^2$ versus $h\nu$ (Fig. 6b) since CoFe_2O_4 and $\text{g-C}_3\text{N}_4$ were direct transition semiconductor materials [27,58]. The E_g values for BCN, 5- $\text{CoFe}_2\text{O}_4/\text{BCN}$, 5- $\text{CoFe}_2\text{O}_4/\text{MCN}$, 5- $\text{CoFe}_2\text{O}_4/\text{CNS}$ and 5- $\text{CoFe}_2\text{O}_4/\text{CNT}$ were estimated to be 2.60, 2.60, 2.86, 2.40 and 2.71 eV, respectively. The 5- $\text{CoFe}_2\text{O}_4/\text{CNS}$ photocatalyst had a narrower bandgap than others, leading to more light generated electrons under visible light irradiation [2]. Notably, CoFe_2O_4 nanoparticles

showed an intense absorption in the range of 200–800 nm, due to the narrow band gap (~ 1.4 eV, Fig. 6b inset). Compared with pure BCN, the absorption edge of 5- $\text{CoFe}_2\text{O}_4/\text{CNS}$ showed an obvious blue shift, which was attributed to the quantum size effect of CNS [59]. Moreover, the red shift of 5- $\text{CoFe}_2\text{O}_4/\text{MCN}$ and 5- $\text{CoFe}_2\text{O}_4/\text{CNT}$ were caused by the quantum size effect of CoFe_2O_4 [60]. A smaller band gap meant the enhanced light harvesting in the visible region [61], suggesting that 5- $\text{CoFe}_2\text{O}_4/\text{CNS}$ had the best photocatalytic properties under visible light irradiation.

The PL spectra analysis was performed to investigate the separation process of the photo-induced electron (e^-)-hole (h^+) pairs [43]. As seen in Fig. 6c, the emission intensity of 5- $\text{CoFe}_2\text{O}_4/\text{BCN}$, 5- $\text{CoFe}_2\text{O}_4/\text{MCN}$, 5- $\text{CoFe}_2\text{O}_4/\text{CNS}$ and 5- $\text{CoFe}_2\text{O}_4/\text{CNT}$ illustrated an obvious decrease in contrast to BCN. Besides, the peak showed ~ 15 nm blue shift after the introduction of CoFe_2O_4 into $\text{g-C}_3\text{N}_4$, which was similar to previous literatures [25]. The blue shift could be attributed to the Burstein-Moss

effect [62,63]. A weaker emission peak intensity represented a lower recombination possibility of photoinduced charge carriers since the recombination of photoexcited electrons and holes afforded the PL emission [64]. The 5-CoFe₂O₄/CNS heterojunction exhibited extremely low PL spectrum intensity, suggesting a noticeable inhibited recombination rate of the photoinduced electrons and holes. It was concluded that the 5-CoFe₂O₄/CNS composites showed higher photocatalytic activity.

In order to further illustrate the excellent activity of 5-CoFe₂O₄/CNS, the transient photocurrent responses (I-t curves) and electrochemical impedance spectra (EIS) experiments were carried out in 0.1 M Na₂SO₄ [25]. As shown in Fig. 6d, 5-CoFe₂O₄/CNS presented a much higher photocurrent density than the second highest sample (5-CoFe₂O₄/CNT, ~0.2 μ A), which meant 5-CoFe₂O₄/CNS had a higher electrons-holes separation efficiency. In addition, the I-t curves of the four photocatalysts almost maintained the same after six ON/OFF illumination cycles, suggesting the good photoelectrochemical stability.

It was known to all, the smaller arc in the EIS Nyquist plot exhibited a lower charge-transfer resistance on the surface of the electrode [2]. From Fig. 6e, the 5-CoFe₂O₄/CNS possessed the smallest arc radius than other three photocatalysts, indicating that 5-CoFe₂O₄/CNS possessed a faster separation ability and 5-CoFe₂O₄/CNT was the second. These results were in good agreement with the PL and UV-vis diffuse reflectance spectra (DRS) analysis, which demonstrated lamellar structure of g-C₃N₄ and loading of CoFe₂O₄ had significant effect to enhance the

photocatalytic performance.

The E_{VB} of CoFe₂O₄ and Bulk g-C₃N₄ were determined by the XPS valence band spectrum. Hence, the E_{VB} of CoFe₂O₄ and BCN were 0.12 eV (Fig. 7a) and 1.90 eV (Fig. 7b), respectively. According to the results of DRS spectra (Fig. 6b), The E_g values for BCN and CoFe₂O₄ were 2.6 eV and 1.4 eV, respectively. The E_{CB} values of BCN and CoFe₂O₄ were calculated according to Eq. (2):

$$E_{VB} = E_{CB} + E_g \quad (2)$$

As a result, The E_{CB} value of BCN was -0.7 eV as well as the E_{CB} value of CoFe₂O₄ was -1.28 eV. According to the E_{CB} and E_{VB} values obtained for CoFe₂O₄ and BCN, the energy band structure of the catalyst before contact was described in Fig. 7c (left).

It is well known that the M-S curve is an effective technique to confirm the semiconductor type of semiconductors. Generally, the M-S plot exhibits a positive slope, and then the semiconductor is regarded as an n-type semiconductor, whereas a p-type semiconductor has a negative slope. As shown in Fig. 6f, the M-S plot of 5-CoFe₂O₄/CNS showed an inverted "V-shape", which confirmed that CoFe₂O₄ and g-C₃N₄ formed p-n heterojunctions.

Generally, the E_f was located near to CB position for n-type semiconductor (about 0.10 eV more negative) and VB for p-type semiconductor (about 0.10 eV more positive) [65,66], respectively. The values of E_f of CoFe₂O₄ and g-C₃N₄ were about 0.02 eV and 0.3 eV, respectively. In addition, upon contact of these two materials, electrons

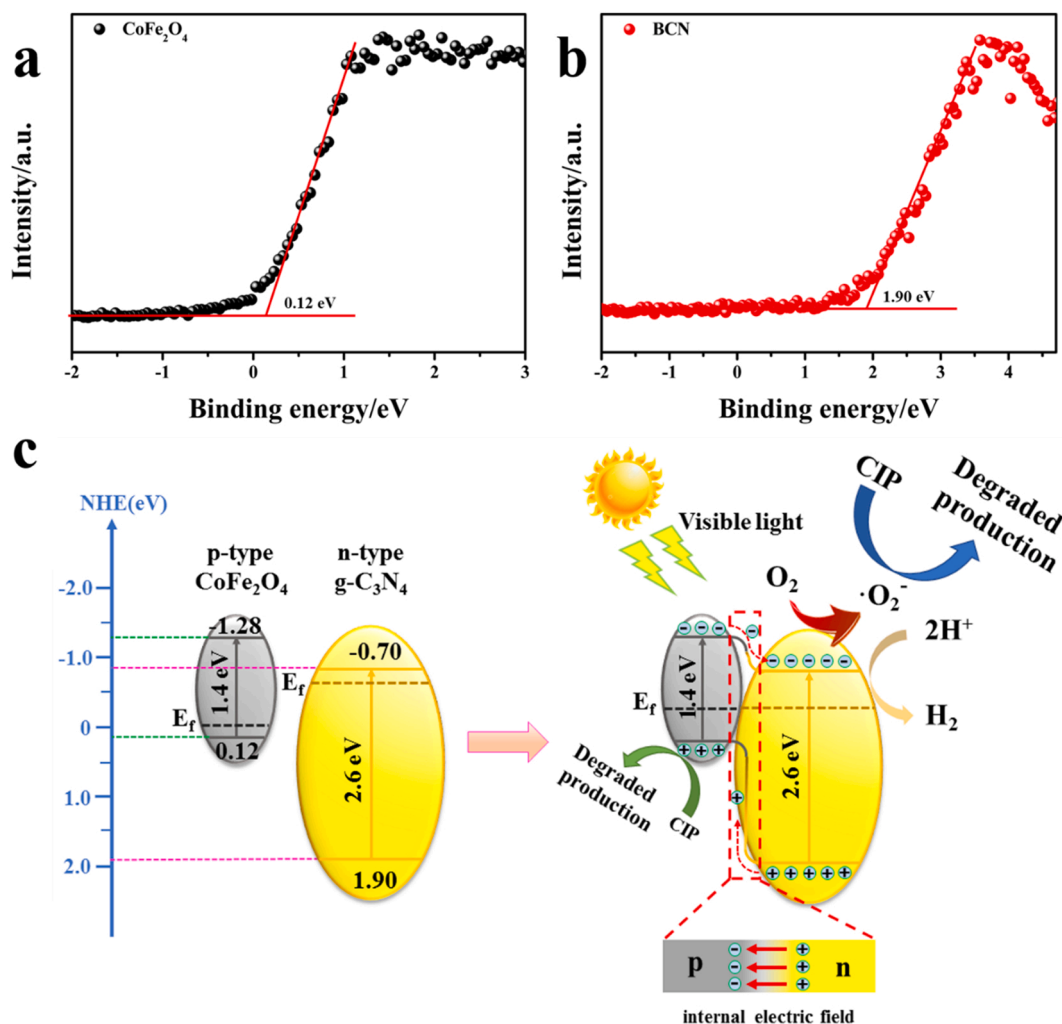


Fig. 7. XPS valence band spectra of CoFe₂O₄ (a), BCN (b) and energy band structure (c) of CoFe₂O₄ and g-C₃N₄ before and after contact and the possible charge transfer process for visible light-irradiated 5-CoFe₂O₄/g-C₃N₄.

were transferred from g-C₃N₄ (with a higher E_F) to CoFe₂O₄ (with a lower one) until both E_F s ultimately reached an equilibrium state [46], as evidenced by the results of above XPS analysis. This phenomenon would cause band bending for both semiconductors, affording the formation of an internal electric field (IEF) at the contact interface (Fig. 7c, right). Driven by the IEF, photogenerated electrons at the CB position of CoFe₂O₄ could transfer easily to the CB position of g-C₃N₄, and photogenerated holes would transfer from the VB position of g-C₃N₄ to VB position of CoFe₂O₄. In this way, electrons and holes were accumulated in the VB position of g-C₃N₄ and CB position of CoFe₂O₄, respectively. Then the photogenerated electron-hole pairs were effectively separated. Therefore, the 5-CoFe₂O₄/CNS p-n junction effectively retarded the recombination of photogenerated electrons and holes, which was verified by the above M-S plots and EIS Nyquist plots. Hence, it could greatly enhance the performance of photocatalytic activity.

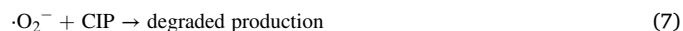
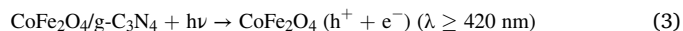
Transient absorption spectroscopy (TAS) was also carried out to reveal the photogenerated electron-hole separation process in the photocatalyst directly. The catalyst concentration was kept constant at 0.2 mg/mL, and all the measurements were performed with a 400 nm pump excitation. TAS spectra revealed a broad bleaching signal below 625 nm and positive absorption features above 625 nm. The negative absorption in the region below 625 nm coincided with the ground-state absorption band of 5-CoFe₂O₄/g-C₃N₄ as seen in the UV-vis spectra of Fig. 6a. A comparable bleach was attributed to stimulated emission in previous TAS investigations on g-C₃N₄ [67]. Also, the distinct positive absorption (625–800 nm) was observed in 5-CoFe₂O₄/g-C₃N₄, which was attributed to photogenerated holes, electrons, or electron-hole pairs (excitons) [68,69].

Considering that the signal at 700 nm was primarily due to photogenerated free electrons, the dynamical decay traces of the photo-excited carriers in 5-CoFe₂O₄/g-C₃N₄ were plotted and probed at 700 nm (Fig. 8a). A three-exponential decay function ($y = y_0 + A_1e^{-x/\tau_1} + A_2e^{-x/\tau_2} + A_3e^{-x/\tau_3}$) was used to describe the carrier dynamics and the corresponding exponential fitted parameters were listed in Fig. 8b. Based on the TAS spectra, a simple model was proposed to understand the charge transfer in 5-CoFe₂O₄/g-C₃N₄. With the use of 400 nm light, inter band excitations would dominate exciting electrons from the VB into the CB. The fast component ($\tau_1 = 1.96$ ps) was assigned to the hole trap, which could effectively eliminate the stimulated emission. The second component at the constant of 86.99 ps suggested that the shallow trap electrons transferred from CoFe₂O₄ to g-C₃N₄ rapidly, which could effectively suppress the deep electron trapping and get the efficient utilization of the shallow trap electrons [70,71]. Moreover, the long-prolonged lifetime of the active species ($\tau_3 = 915.23$ ps) could be ascribed to the recombination of shallow trapping electron and hole, which resulted in high photocatalytic activities.

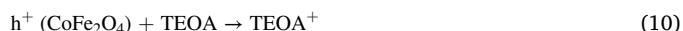
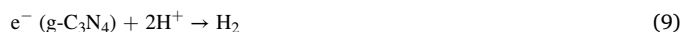
Obviously, the photocatalytic activity could be improved by changing the morphology of the photocatalyst. It could be attributed to the

fact that the surface area and the amounts of active sites might be increased by fabricating different morphologies of photocatalysts, which was verified by the N₂ adsorption-desorption isotherms and the TEM images. In addition, the results of PL spectra, I-t curves and EIS plots also confirmed that photocatalysts with different morphologies had significant differences in the optical and electrochemical properties.

Based on the obtained results, the CIP degradation process in 5 wt% CoFe₂O₄/g-C₃N₄ system (Fig. 7c, right) could be proposed as follows [46]:



The photogeneration of electron/hole pairs over CoFe₂O₄ was occurred with the irradiation of CoFe₂O₄/g-C₃N₄ by visible light ($\lambda \geq 420$ nm) (Eq. (3)). The electrons in the CB position of CoFe₂O₄ would migrate to that of g-C₃N₄ (Eq. (4)) and the holes moved to the opposite direction (Eq. (5)), owing to the presence of an IEF in the p-n type junction. Subsequently, the electrons on the surface of CoFe₂O₄/g-C₃N₄ reacted with O₂ to afford $\cdot\text{O}_2^-$ (Eq. (6)), which could directly oxidize CIP (Eq. (7)). In addition, part of the holes might participate in the oxidize of CIP (Eq. (8)).



Similarly, the electrons trapped by g-C₃N₄ would participate in the reduction with the help of Pt as the cocatalyst (Eq. (9)). The hole at the VB position of CoFe₂O₄ would be preserved for the oxidation of TEOA (Eq. (3)).

4. Conclusion

A series of CoFe₂O₄/g-C₃N₄ photocatalysts with p-n heterojunctions were synthesized for FQs removal and H₂ evolution. The morphology of g-C₃N₄ played a vital role in the formation of p-n heterojunctions. Photocatalytic activities of synthesized catalysts decreased as the following order: 5-CoFe₂O₄/CNS > 5-CoFe₂O₄/CNT > 5-CoFe₂O₄/BCN > 5-CoFe₂O₄/MCN. The high photocatalytic performance of p-n CoFe₂O₄/CNS heterojunction could be attributed to a larger specific surface area, narrow band gap and internal electric field at the contact

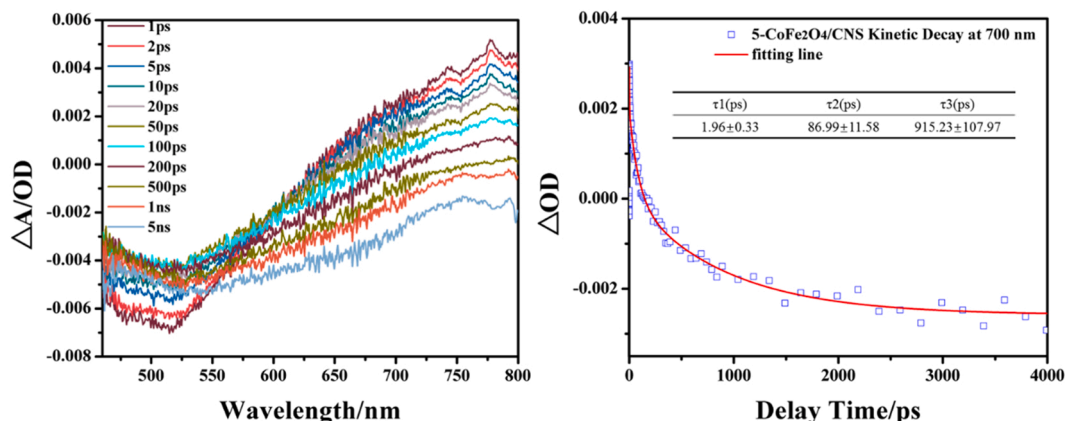


Fig. 8. The TAS spectra of 5-CoFe₂O₄/g-C₃N₄ (a) and experimental decay kinetic (b) monitored under 700 nm of 5-CoFe₂O₄/g-C₃N₄.

interface, thereby promoting more photo-generated electrons, a faster separation ability and noticeable inhibited recombination rate. 5-CoFe₂O₄/CNS presented the highest *k* value in photocatalytic degradation, which was about 2.33 times higher than 5-CoFe₂O₄/MCN. The reaction rate catalyzed by 5-CoFe₂O₄/CNS was 2.6 and 10 times higher than that of 5-CoFe₂O₄/MCN and CNS in H₂ evolution, respectively. The apparent rate constant of acousto-optic microreactor was 7.2 and 30 times higher than the quartz glass tube and batch experiment, respectively.

CRedit authorship contribution statement

Wei He: Investigation, Methodology, Writing – original draft. **Liang Liu:** Investigation, Formal analysis, Data curation. **Tingting Ma:** Validation. **Huimin Han:** Validation. **Jiajing Zhu:** Formal analysis. **Yingpei Liu:** Data curation. **Zheng Fang:** Writing – review & editing. **Zhao Yang:** Writing – review & editing. **Kai Guo:** Supervision, Writing – review & editing.

Declaration of Competing Interest

The authors declare that they have no known competing financial interests or personal relationships that could have appeared to influence the work reported in this paper.

Acknowledgement

The research has been supported by The National Natural Science Foundation of China (21908094, 22178168, 21776130 and 22078150); The National Key Research and Development Program of China (2021YFC2101900); The Top-notch Academic Programs Project of Jiangsu Higher Education Institutions.

Appendix A. Supporting information

Supplementary data associated with this article can be found in the online version at doi:10.1016/j.apcatb.2022.121107.

References

- [1] G. Liu, P. Niu, C. Sun, S.C. Smith, Z. Chen, G.Q. Lu, H.-M. Cheng, Unique electronic structure induced high photoreactivity of sulfur-doped graphitic C₃N₄, *J. Am. Chem. Soc.* 132 (2010) 11642–11648.
- [2] W. Wang, Z. Zeng, G. Zeng, C. Zhang, R. Xiao, C. Zhou, W. Xiong, Y. Yang, L. Lei, Y. Liu, D. Huang, M. Cheng, Y. Yang, Y. Fu, H. Luo, Y. Zhou, Sulfur doped carbon quantum dots loaded hollow tubular g-C₃N₄ as novel photocatalyst for destruction of *Escherichia coli* and tetracycline degradation under visible light, *Chem. Eng. J.* 378 (2019), 122132.
- [3] B. Shao, Z. Liu, G. Zeng, Z. Wu, Y. Liu, M. Cheng, M. Chen, Y. Liu, W. Zhang, H. Feng, Nitrogen-doped hollow mesoporous carbon spheres modified g-C₃N₄/Bi₂O₃ direct dual semiconductor photocatalytic system with enhanced antibiotics degradation under visible light, *ACS Sustain. Chem. Eng.* 6 (2018) 16424–16436.
- [4] J. Fu, J. Yu, C. Jiang, B. Cheng, g-C₃N₄-based heterostructured photocatalysts, *Adv. Energy Mater.* 8 (2018), 1701503.
- [5] J. Dai, J. Song, Y. Qiu, J. Wei, Z. Hong, L. Li, H. Yang, Gold nanoparticle-decorated g-C₃N₄ nanosheets for controlled generation of reactive oxygen species upon 670 nm laser illumination, *ACS Appl. Mater. Interfaces* 11 (2019) 10589–10596.
- [6] T. Zeng, S. Li, Y. Shen, H. Zhang, H. Feng, X. Zhang, L. Li, Z. Cai, S. Song, Sodium doping and 3D honeycomb nanoarchitecture: Key features of covalent triazine-based frameworks (CTF) organocatalyst for enhanced solar-driven advanced oxidation processes, *Appl. Catal. B: Environ.* 257 (2019), 117915.
- [7] N. Fajrina, M. Tahir, Engineering approach in stimulating photocatalytic H₂ production in a slurry and monolithic photoreactor systems using Ag-bridged Z-scheme pCN/TiO₂ nanocomposite, *Chem. Eng. J.* 374 (2019) 1076–1095.
- [8] C. Liu, L. Liu, X. Tian, Y. Wang, R. Li, Y. Zhang, Z. Song, B. Xu, W. Chu, F. Qi, A. Ikhtaq, Coupling metal-organic frameworks and g-C₃N₄ to derive Fe@N-doped graphene-like carbon for peroxymonosulfate activation: upgrading framework stability and performance, *Appl. Catal. B: Environ.* 255 (2019), 117763.
- [9] S.C. Yan, Z.S. Li, Z.G. Zou, Photodegradation of rhodamine B and methyl orange over boron-doped g-C₃N₄ under visible light irradiation, *Langmuir* 26 (2010) 3894–3901.
- [10] Y. Wang, Y. Di, M. Antonietti, H. Li, X. Chen, X. Wang, Excellent visible-light photocatalysis of fluorinated polymeric carbon nitride solids, *Chem. Mater.* 22 (2010) 5119–5121.
- [11] G. Dong, K. Zhao, L. Zhang, Carbon self-doping induced high electronic conductivity and photoreactivity of g-C₃N₄, *Chem. Commun.* 48 (2012) 6178–6180.
- [12] T. Xu, D. Wang, L. Dong, H. Shen, W. Lu, W. Chen, Graphitic carbon nitride co-modified by zinc phthalocyanine and graphene quantum dots for the efficient photocatalytic degradation of refractory contaminants, *Appl. Catal. B: Environ.* 244 (2019) 96–106.
- [13] J. Ran, T.Y. Ma, G. Gao, X.-W. Du, S.Z. Qiao, Porous P-doped graphitic carbon nitride nanosheets for synergistically enhanced visible-light photocatalytic H₂ production, *Energy Environ. Sci.* 8 (2015) 3708–3717.
- [14] P. Qiu, C. Xu, H. Chen, F. Jiang, X. Wang, R. Lu, X. Zhang, One step synthesis of oxygen doped porous graphitic carbon nitride with remarkable improvement of photo-oxidation activity: Role of oxygen on visible light photocatalytic activity, *Appl. Catal. B: Environ.* 206 (2017) 319–327.
- [15] T. Su, Z.D. Hood, M. Naguib, L. Bai, S. Luo, C.M. Rouleau, I.N. Ivanov, H. Ji, Z. Qin, Z. Wu, 2D/2D heterojunction of Ti₃C₂/g-C₃N₄ nanosheets for enhanced photocatalytic hydrogen evolution, *Nanoscale* 11 (2019) 8138–8149.
- [16] X. Yang, L. Tian, X. Zhao, H. Tang, Q. Liu, G. Li, Interfacial optimization of g-C₃N₄-based Z-scheme heterojunction toward synergistic enhancement of solar-driven photocatalytic oxygen evolution, *Appl. Catal. B-Environ.* 244 (2019) 240–249.
- [17] Y. Liu, X. Zeng, X. Hu, J. Hu, Z. Wang, Y. Yin, C. Sun, X. Zhang, Two-dimensional g-C₃N₄/TiO₂ nanocomposites as vertical Z-scheme heterojunction for improved photocatalytic water disinfection, *Catal. Today* 335 (2019) 243–251.
- [18] S. Liu, S. Wang, Y. Jiang, Z. Zhao, G. Jiang, Z. Sun, Synthesis of Fe₂O₃ loaded porous g-C₃N₄ photocatalyst for photocatalytic reduction of dinitrogen to ammonia, *Chem. Eng. J.* 373 (2019) 572–579.
- [19] Y. Wang, L. Guo, Y. Zeng, H. Guo, S. Wan, M. Ou, S. Zhang, Q. Zhong, Amino-assisted NH₂-UiO-66 anchored on porous g-C₃N₄ for enhanced visible-light-driven CO₂ reduction, *ACS Appl. Mater. Interfaces* 11 (2019) 30673–30681.
- [20] D. Liu, S. Zhang, J. Wang, T. Peng, R. Li, Direct Z-scheme 2D/2D photocatalyst based on ultrathin g-C₃N₄ and WO₃ nanosheets for efficient visible-light-driven H₂ generation, *ACS Appl. Mater. Inter.* 11 (2019) 27913–27923.
- [21] J. Zheng, L. Zhang, Designing 3D magnetic peony flower-like cobalt oxides/g-C₃N₄ dual Z-scheme photocatalyst for remarkably enhanced sunlight driven photocatalytic redox activity, *Chem. Eng. J.* 369 (2019) 947–956.
- [22] J. Xu, L. Zhang, R. Shi, Y. Zhu, Chemical exfoliation of graphitic carbon nitride for efficient heterogeneous photocatalysis, *J. Mater. Chem. A* 1 (2013) 14766–14772.
- [23] W. Wang, G. Li, T. An, D.K.L. Chan, J.C. Yu, P.K. Wong, Photocatalytic hydrogen evolution and bacterial inactivation utilizing sonochemical-synthesized g-C₃N₄/red phosphorus hybrid nanosheets as a wide-spectral-responsive photocatalyst: The role of type I band alignment, *Appl. Catal. B: Environ.* 238 (2018) 126–135.
- [24] Z. Mo, H. Xu, Z. Chen, X. She, Y. Song, J. Wu, P. Yan, L. Xu, Y. Lei, S. Yuan, H. Li, Self-assembled synthesis of defect-engineered graphitic carbon nitride nanotubes for efficient conversion of solar energy, *Appl. Catal. B: Environ.* 225 (2018) 154–161.
- [25] R. Li, M. Cai, Z. Xie, Q. Zhang, Y. Zeng, H. Liu, G. Liu, W. Lv, Construction of heterostructured CuFe₂O₄/g-C₃N₄ nanocomposite as an efficient visible light photocatalyst with peroxydisulfate for the organic oxidation, *Appl. Catal. B-Environ.* 244 (2019) 974–982.
- [26] Y. Zeng, N. Guo, Y. Song, Y. Zhao, H. Li, X. Xu, J. Qiu, H. Yu, Fabrication of Z-scheme magnetic MoS₂/CoFe₂O₄ nanocomposites with highly efficient photocatalytic activity, *J. Colloid Interface Sci.* 514 (2018) 664–674.
- [27] Z. Shao, T. Zeng, Y. He, D. Zhang, X. Pu, A novel magnetically separable CoFe₂O₄/Cd_{0.9}Zn_{0.1}S photocatalyst with remarkably enhanced H₂ evolution activity under visible light irradiation, *Chem. Eng. J.* 359 (2019) 485–495.
- [28] M. Lu, H. Li, W. Han, Y. Wang, W. Shi, J. Wang, H. Chen, H. Li, B. Zhang, W. Zhang, W. Zheng, Integrated MXene/CoFe₂O₄ electrodes with multi-level interfacial architectures for synergistic lithium-ion storage, *Nanoscale* 11 (2019) 15037–15042.
- [29] J. Liu, R. Meng, J. Li, P. Jian, L. Wang, R. Jian, Achieving high-performance for catalytic epoxidation of styrene with uniform magnetically separable CoFe₂O₄ nanoparticles, *Appl. Catal. B: Environ.* 254 (2019) 214–222.
- [30] J. Tan, N. Tian, Z. Li, J. Li, X. Yao, M. Vakili, Y. Lu, T. Zhang, Intrinsic defect engineering in graphitic carbon nitride for photocatalytic environmental purification: a review to fill existing knowledge gaps, *Chem. Eng. J.* 421 (2021), 127729.
- [31] X. Li, Y. Zhao, L. Ding, D. Wang, Q. Guo, Z. Li, H. Luo, D. Zhang, Y. Yu, Enhancing capacity and stability by CoFe₂O₄ modified g-C₃N₄ composite for lithium-oxygen batteries, *Nanomaterials* 11 (2021) 1088.
- [32] M.W. Kadi, R.M. Mohamed, A.A. Ismail, D.W. Bahnemann, Decoration of g-C₃N₄ nanosheets by mesoporous CoFe₂O₄ nanoparticles for promoting visible-light photocatalytic Hg (II) reduction, *Colloid Surf. A* 603 (2020), 125206.
- [33] W. Chen, D. Jiang, M. Zhu, T. Shi, H. Li, K. Wang, An effective strategy for fabricating highly dispersed nanoparticles on O-C₃N₄ with enhanced electrocatalytic activity and stability, *J. Alloy. Compd.* 741 (2018) 1203–1211.
- [34] Q. Zheng, Y. Xu, Y. Wan, J. Wu, X. Hu, X. Yao, Synthesis of CoFe₂O₄-modified g-C₃N₄ with enhanced photocatalytic performance for nitrogen fixation, *J. Nanopart. Res.* 22 (2020) 301.
- [35] D. Schieppati, F. Galli, M.L. Peyot, V. Yargeau, C.L. Bianchi, D.C. Boffito, An ultrasound-assisted photocatalytic treatment to remove an herbicidal pollutant from wastewaters, *Ultrason. Sonochem.* 54 (2019) 302–310.
- [36] A.V. Karim, A. Shrivastav, Degradation of ciprofloxacin using photo, sono, and sonophotocatalytic oxidation with visible light and low-frequency ultrasound: degradation kinetics and pathways, *Chem. Eng. J.* 392 (2020), 124853.

- [37] B. Lin, J.L. Hedrick, N.H. Park, R.M. Waymouth, Programmable high-throughput platform for the rapid and scalable synthesis of polyester and polycarbonate libraries, *J. Am. Chem. Soc.* 141 (2019) 8921–8927.
- [38] N.F.F. Moreira, M.J. Sampaio, A.R. Ribeiro, C.G. Silva, J.L. Faria, A.M.T. Silva, Metal-free g-C₃N₄ photocatalysis of organic micropollutants in urban wastewater under visible light, *Appl. Catal. B: Environ.* 248 (2019) 184–192.
- [39] F. Ahmedchekkat, M.S. Medjram, M. Chiha, A.M.A. Al-bsoul, Sonophotocatalytic degradation of rhodamine B using a novel reactor geometry: effect of operating conditions, *Chem. Eng. J.* 178 (2011) 244–251.
- [40] P.R. Gogate, A.B. Pandit, Sonophotocatalytic reactors for wastewater treatment: a critical review, *AIChE J.* 50 (2004) 1051–1079.
- [41] W. He, Y. Gao, G. Zhu, H. Wu, Z. Fang, K. Guo, Microfluidic synthesis of fatty acid esters: Integration of dynamic combinatorial chemistry and scale effect, *Chem. Eng. J.* 381 (2020), 122721.
- [42] N.L. Stock, J. Peller, K. Vinodgopal, P.V. Kamat, Combinative sonolysis and photocatalysis for textile dye degradation, *Environ. Sci. Technol.* 34 (2000) 1747–1750.
- [43] W. Chang, W. Xue, E. Liu, J. Fan, B. Zhao, Highly efficient H₂ production over NiCo₂O₄ decorated g-C₃N₄ by photocatalytic water reduction, *Chem. Eng. J.* 362 (2019) 392–401.
- [44] S. Yang, Y. Gong, J. Zhang, Li Zhan, L. Ma, Z. Fang, R. Vajtai, X. Wang, P. M. Ajayan, Exfoliated graphitic carbon nitride nanosheets as efficient catalysts for hydrogen evolution under visible light, *Adv. Mater.* 25 (2013) 2452–2456.
- [45] H. Li, T. Hu, R. Zhang, J. Liu, W. Hou, Preparation of solid-state Z-scheme Bi₂MoO₆/MO (M=Cu, Co³⁺/4, or Ni) heterojunctions with internal electric field-improved performance in photocatalysis, *Appl. Catal. B-Environ.* 188 (2016) 313–323.
- [46] Y. Huang, D. Zhu, Q. Zhang, Y. Zhang, J.-j. Cao, Z. Shen, W. Ho, S.C. Lee, Synthesis of a Bi₂O₃/ZnFe₂O₄ heterojunction with enhanced photocatalytic activity for visible light irradiation-induced NO removal, *Appl. Catal. B: Environ.* 234 (2018) 70–78.
- [47] J. Liu, S. Fang, R. Jian, F. Wu, P. Jian, Silylated Pd/Ti-MCM-41 catalyst for the selective production of propylene oxide from the oxidation of propylene with cumene hydroperoxide, *Powder Technol.* 329 (2018) 19–24.
- [48] J. Zhu, P. Xiao, H. Li, S.A.C. Carabineiro, Graphitic carbon nitride: synthesis, properties, and applications in catalysis, *ACS Appl. Mater. Interfaces* 6 (2014) 16449–16465.
- [49] C. Hu, F. Chen, Y. Wang, N. Tian, T. Ma, Y. Zhang, H. Huang, Exceptional cocatalyst-free photo-enhanced piezocatalytic hydrogen evolution of carbon nitride nanosheets from strong in-plane polarization, *Adv. Mater.* 33 (2021), 2101751.
- [50] X. Hu, X. Hu, Q. Peng, L. Zhou, X. Tan, L. Jiang, C. Tang, H. Wang, S. Liu, Y. Wang, Z. Ning, Mechanisms underlying the photocatalytic degradation pathway of ciprofloxacin with heterogeneous TiO₂, *Chem. Eng. J.* 380 (2020), 122366.
- [51] X.-J. Wen, C.-G. Niu, L. Zhang, C. Liang, H. Guo, G.-M. Zeng, Photocatalytic degradation of ciprofloxacin by a novel Z-scheme CeO₂-Ag/AgBr photocatalyst: Influencing factors, possible degradation pathways, and mechanism insight, *J. Catal.* 358 (2018) 141–154.
- [52] H.-s. Ou, J.-s. Ye, S. Ma, C.-h. Wei, N.-y. Gao, J.-z. He, Degradation of ciprofloxacin by UV and UV/H₂O₂ via multiple-wavelength ultraviolet light-emitting diodes: effectiveness, intermediates and antibacterial activity, *Chem. Eng. J.* 289 (2016) 391–401.
- [53] K. Liu, Z. Tong, Y. Muhammad, G. Huang, H. Zhang, Z. Wang, Y. Zhu, R. Tang, Synthesis of sodium dodecyl sulfate modified BiOBr/magnetic bentonite photocatalyst with three-dimensional parterre like structure for the enhanced photodegradation of tetracycline and ciprofloxacin, *Chem. Eng. J.* 388 (2020), 124374.
- [54] X. Yu, J. Qu, Z. Yuan, P. Min, S. Hao, Z. Zhu, X. Li, D. Yang, Z. Yu, Anisotropic CoFe₂O₄@graphene hybrid aerogels with high flux and excellent stability as building blocks for rapid catalytic degradation of organic contaminants in a flow-type setup, *ACS Appl. Mater. Interfaces* 11 (2019) 34222–34231.
- [55] L. He, M. Fei, J. Chen, Y. Tian, Y. Jiang, Y. Huang, K. Xu, J. Hu, Z. Zhao, Q. Zhang, H. Ni, L. Chen, Graphitic C₃N₄ quantum dots for next-generation QLED displays, *Mater. Today* 22 (2019) 76–84.
- [56] P. Wu, J. Wang, J. Zhao, L. Guo, F.E. Osterloh, Structure defects in g-C₃N₄ limit visible light driven hydrogen evolution and photovoltage, *J. Mater. Chem. A* 2 (2014) 20338–20344.
- [57] Y. Huang, W. Fan, B. Long, H. Li, F. Zhao, Z. Liu, Y. Tong, H. Ji, Visible light Bi₂S₃/Bi₂O₃/Bi₂O₃CO₃ photocatalyst for effective degradation of organic pollutants, *Appl. Catal. B: Environ.* 185 (2016) 68–76.
- [58] G. Fan, B. Du, J. Zhou, W. Yu, Z. Chen, S. Yang, Stable Ag₂O/g-C₃N₄ p-n heterojunction photocatalysts for efficient inactivation of harmful algae under visible light, *Appl. Catal. B: Environ.* 265 (2020), 118610.
- [59] Q. Han, B. Wang, J. Gao, Z. Cheng, Y. Zhao, Z. Zhang, L. Qu, Atomically thin mesoporous nanomesh of graphitic C₃N₄ for high-efficiency photocatalytic hydrogen evolution, *ACS Nano* 10 (2016) 2745–2751.
- [60] Z. Han, Y. Yu, W. Zheng, Y. Cao, The band structure and photocatalytic mechanism for a CeO₂-modified C₃N₄ photocatalyst, *New J. Chem.* 41 (2017) 9724–9730.
- [61] G. Liu, G. Zhao, W. Zhou, Y. Liu, H. Pang, H. Zhang, D. Hao, X. Meng, P. Li, T. Kako, J. Ye, In situ bond modulation of graphitic carbon nitride to construct p-n homojunctions for enhanced photocatalytic hydrogen production, *Adv. Funct. Mater.* 26 (2016) 6822–6829.
- [62] A.C. Pradhan, T. Uyar, Morphological control of mesoporosity and nanoparticles within Co₃O₄-CuO electrospun nanofibers: quantum confinement and visible light photocatalysis performance, *ACS Appl. Mater. Interface* 9 (2017) 35757–35774.
- [63] D.M. Fryauf, J. Zhang, K.J. Norris, J.J. Diaz Leon, M.M. Oye, M. Wei, N. P. Kobayashi, Photoluminescence blue shift of indium phosphide nanowire networks with aluminum oxide coating, *Phys. Status Solidi - RRL* 8 (2014) 663–667.
- [64] Y. Yang, J. Wen, J. Wei, R. Xiong, J. Shi, C. Pan, Polypyrrole-decorated Ag-TiO₂ nanofibers exhibiting enhanced photocatalytic activity under visible-light illumination, *ACS Appl. Mater. Interfaces* 5 (2013) 6201–6207.
- [65] S. Saha, G. Das, J. Thote, R. Banerjee, Photocatalytic metal-organic framework from CdS quantum dot incubated luminescent metallohydrogel, *J. Am. Chem. Soc.* 136 (2014) 14845–14851.
- [66] Y. Jia, J. Yang, D. Zhao, H. Han, C. Li, A novel Sr₂CuInO₃S p-type semiconductor photocatalyst for hydrogen production under visible light irradiation, *J. Energy Chem.* 23 (2014) 420–426.
- [67] C. Merschjann, S. Tschierlei, T. Tyborski, K. Kailasam, S. Lochbrunner, Complementing graphenes: 1D interplanar charge transport in polymeric graphitic carbon nitrides, *Adv. Mater.* 27 (2016) 7993–7999.
- [68] R. Godin, Y. Wang, M.A. Zwijnenburg, J. Tang, J.R. Durrant, Time-resolved spectroscopic investigation of charge trapping in carbon nitrides photocatalysts for hydrogen generation, *J. Am. Chem. Soc.* 139 (2017) 5216.
- [69] H. Zhang, Y. Chen, R. Lu, R. Li, A. Yu, Charge carrier kinetics of carbon nitride colloid: a femtosecond transient absorption spectroscopy study, *Phys. Chem. Chem. Phys.* 22 (2016) 14904–14910.
- [70] B. Wwa, T.A. Ying, B. Ld, W.B. Zhen, B. Zy, B. Wkc, C. Zi, D. Rzb, B. Dlp, E. Gla, Femtosecond time-resolved spectroscopic observation of long-lived charge separation in bimetallic sulfide/g-C₃N₄ for boosting photocatalytic H₂ evolution, *Appl. Catal. B: Environ.* 282 (2021), 119568.
- [71] K.M. Adnan, M. Partha, A.O. Maher, A. Khalid, I. Hicham, Electron transfer of the metal/semiconductor system in photocatalysis, *J. Phys. Chem. C* 122 (2018) 16779–16787.